Generation of non-stationary stochastic fields using Generative Adversarial Networks with limited training data

Alhasan Abdellatif [*1], Ahmed H. Elsheikh[†1], Daniel Busby[2], and Philippe Berthet[2]

[1]Heriot-Watt University
[2]TotalEnergies

May 12, 2022

Abstract

In the context of generating geological facies conditioned on observed data, samples corresponding to all possible conditions are not generally available in the training set and hence the generation of these realizations depends primary on the generalization capability of the trained generative model. The problem becomes more complex when applied on non-stationary fields. In this work, we investigate the problem of training Generative Adversarial Networks (GANs) models against a dataset of geological channelized patterns that has a few non-stationary spatial modes and examine the training and self-conditioning settings that improve the generalization capability at new spatial modes that were never seen in the given training set. The developed training method allowed for effective learning of the correlation between the spatial conditions (i.e. non-stationary maps) and the realizations implicitly without using additional loss terms or solving a costly optimization problem at the realization generation phase. Our models, trained on real and artificial datasets were able to generate geologically-plausible realizations beyond the training samples with a strong correlation with the target maps.

Keywords: Generative Adversarial Networks (GANs), Non-stationary Stochastic Fields, Multipoint Geostatistics.

1   Introduction

Generating non-stationary stochastic fields has many applications in engineering and geosciences. In this paper, we focus on modeling facies at the reservoir scale as an essential step for addressing uncertainty quantification or inverse problems in the subsurface Multiple point statistics (MPS) algorithms Mariethoz et al. (2010); Strebelle (2002) were designed for geostatistical simulation based on a training image. However, MPS algorithms suffer from many limitations such as the high computational cost Li et al. (2016), limited variability Emery & Lantuéjoul (2014) and inability to model complex non-stationary patterns T. Zhang et al. (2019).

Following the success of deep learning in computer vision, recent published work have considered deep generative models such as Generative Adversarial Networks (GANs) Goodfellow et al. (2014) for generation of stochastic fields. For example, GANs were used to model 3D structure of porous media Mosser et al. (2017), low-dimensional latent vector of GANs was utilized to perform parametrization of the spatial permeability fields in the subsurface Chan & Elsheikh (2017) and geostatistical inversion was performed after training a GAN model on 2D and 3D categorical samples Laloy et al. (2018).

---

[*]aa519@hw.ac.uk

[†]a.elsheikh@hw.ac.uk

GANs have been used to generate geological realizations conditioned on hard data (e.g., point measurements at wells) and soft data (e.g., probability maps). Approaches for generation of conditioned stochastic realizations could be classified into two categories: post-GANs and concurrent-GANs. In post-GANs approaches, a new optimization problem is solved after training a GANs generator where the latent vector is searched to find realizations that match the target data. For example, gradient descent method was used in Dupont et al. (2018); T. Zhang et al. (2019), a Markov Chain Monte Carlo sampling algorithms were used in Nesvold & Mukerji (2019); Laloy et al. (2018) and Chan & Elsheikh (2019) trained an inference network to map the normally distributed outputs to a distribution of latent vectors that satisfies the required conditions. The main drawback of using post-GANs approaches is the additional cost needed to solve the second optimization problem which can often be expensive. In addition, this additional computation work will be needed to solve different problems for every new observed data (e.g. new condition).

In concurrent-GANs approaches, the training of GANs is modified to pass the conditional data to the GANs generator network. After training, the trained generator can then simulate realizations based on the input data without the need to solve another optimization problem. Cycle-consistent GANs Zhu et al. (2017) has been used for domain mapping, for example mapping between physical parameters and model state variables Sun (2018) and mapping between seismic data and geological model Mosser et al. (2018). In Zhong et al. (2019), a GANs model with a U-net architecture Ronneberger et al. (2015) was used to map high-dimensional input to CO_2 saturation maps. However, the one-to-one mapping using Cycle-GANs or U-net architecture is not suitable for generating multiple facies conditioned on observed data. In Abdellatif et al. (2022), conditional GANs were used to generate unrepresented proportions of geological facies.

In Song et al. (2021b), condition-based loss functions were used to condition facies on hard data and global features and later they extended the method for spatial probability maps in Song et al. (2021a). However, condition-based losses relies on designing manual functions that compute the consistency between the generated samples and target conditions (e.g., computing facies frequency for the generated realizations to mimic real probability maps Song et al. (2021a)). Conceptually, this is different than GANs, where the learning is done implicitly from the training data by joint learning of both the generator and the discriminator which tells what is good versus bad samples. In addition, including additional losses in GAN relies on careful weighting between the condition losses and the original loss in GANs which requires extensive hyperparameters search.

In all the published work it is usually assumed that a training set with samples of various and diverse characteristics is available for training GANs. However, this assumption is not true in many cases especially when the characteristics of actual reservoirs differ significantly from those of the available training samples. In this work, we examine the generalization capability of a GANs model to generate geological facies with unrepresented spatial modes in the training set. Each mode is a 2D map that describes the distribution of facies proportions across the spatial domain. To model the different modes, we utilized conditional GANs (cGANs) Mirza & Osindero (2014) where each spatial mode is provided as a conditioning map to the neural networks. By letting the spatial maps modulate the generator layers through the SPADE algorithm Park et al. (2019), the GANs models learned the correlation between the spatial conditions and the samples implicitly and we were able to generate new realizations that match spatial maps beyond the training samples. Further, the developed training approach solves a single optimization problem (i.e., a concurrent-GANs method) without using condition-based losses and hence there is no need to design condition-consistency functions or to perform careful hyperparameter search for balancing weights.

The rest of the paper is organized as follows: in section 2, we discuss the algorithm of conditional GANs used in our experiments and we present the training datasets and the implementation details. In section 3, the results of the experiments are shown. Finally, conclusions are provided in section 4.

2 Method and Materials

2.1 Method

Generative adversarial networks (GANs) Goodfellow et al. (2014) are trained to learn the underlying distribution of training samples. It consists of two convolutional neural networks: a generator G and a discriminator D. The generator maps a random noise z to a realization $G(z)$ while the discriminator takes samples from the real and the generated sets and is optimized to output the probability of the samples being real (i.e., not generated by the generator). The generator is then optimized such that the generated samples have high probability $D(G(z))$. The two networks are trained in an adversarial setting defined by the objective function $V(G, D)$:

$$\min_G \max_D V(G, D) = \mathbb{E}_{x \sim p_x}[\log D(x)] + \mathbb{E}_{z \sim p_z}[\log(1 - D(G(z)))]. \tag{1}$$

In order to direct the generated samples to match a particular spatial map $\mathbf{M}$, we utilized conditional GANs Mirza & Osindero (2014), where the condition $\mathbf{M}$ is passed to both the generator network G and discriminator network D during training. Similar to the concurrent-GANs methods, after training we can generate multiple realizations conditioned on $\mathbf{M}$ by simply passing $\mathbf{M}$ and different latent z vectors to the generator without solving a new optimization problem. The discriminator would then output the conditional probability of the sample being real given its input map. The objective function of conditional GANs is then:

$$\min_G \max_D V(G, D) = \mathbb{E}_{x \sim p_x}[\log D(x|\mathbf{M})] + \mathbb{E}_{z \sim p_z}[\log(1 - D(G(z, \mathbf{M})|\mathbf{M}))]. \tag{2}$$

To accommodate for the spatial nature of the map, we followed the spatially adaptive denormalization (SPADE) conditioning method developed in Park et al. (2019), where a segmentation mask is used to modulate the generator layers such that it could generate natural images based on the mask.

In our work, we replaced the categorical mask by a continuous map representing the spatial proportions of the channels. First, for each layer i and channel c in the generator, each activation $h_{i,c,x,y}$ is normalized using the mean $\mu_{i,c}$ and standard variation $\sigma_{i,c}$ computed over both batch instances and channel spatial locations. The result is then de-normalized spatially, i.e., for each spatial position in the channel, using learnable parameters γ and β which are functions of the map $\mathbf{M}$. The calculation of SPADE algorithm is shown in following equation:

$$\hat{h}_{i,c,x,y}(\mathbf{M}) = \gamma_{i,c,x,y}(\mathbf{M}) \frac{h_{i,c,x,y} - \mu_{i,c}}{\sigma_{i,c}} + \beta_{i,c,x,y}(\mathbf{M}). \tag{3}$$

The learnable parameters γ and β are obtained using two successive convolutional layers directly applied to the map $\mathbf{M}$. We can then modify the spatial proportions of the generated facies by modifying $\mathbf{M}$ which will in turn modulate the generator activations through γ and β. Since each layer of the generator operates at different resolution, the map $\mathbf{M}$ is down-sampled (or up-sampled in case $\mathbf{M}$ has a lower resolution) to match the resolution of the feature channels at each layer.

Both the generator and the discriminator is based the ResNet architecture He et al. (2016) following Gulrajani et al. (2017). The discriminator halves the features spatial resolution and doubles the number of features channels after each layer before it outputs a single value indicating the probability if the image being real. Features computed from the map $\mathbf{M}$, using convolutional layers, are concatenated with spatial features computed from the input image at an intermediate layer of the discriminator. The intermediate layer is chosen such that its resolution matches the resolution of $\mathbf{M}$. For example, if the input images are of resolution 64×64 and $\mathbf{M}$ is 4×4 then the concatenation is done at the fourth layer.

(a) Artificial dataset of 3 different facies
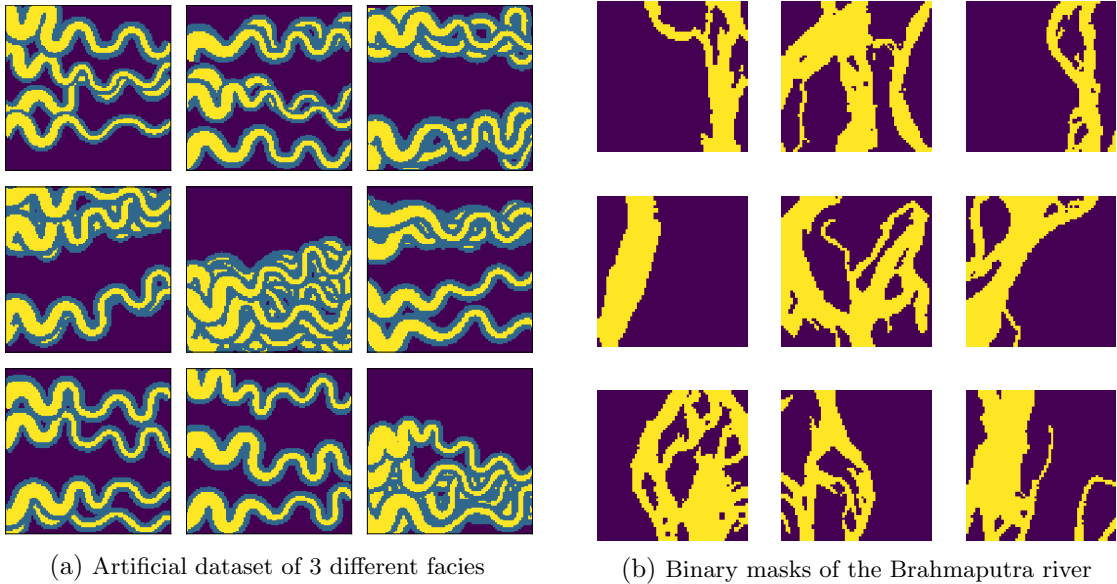
(b) Binary masks of the Brahmaputra river

Figure 1: Training datasets used to train GANs models

2.2 Datasets

We used two datasets: a) an artificial dataset of 3 facies: channels, levees and background b) a dataset of masks of the Brahmaputra river with binary facies: channels and background, as shown in figures 1a and 1b, respectively. The non-stationarity in the two datasets are due to the variations in the channels proportions across the spatial domain. For example in figure 1a, the channel proportions is large in the left side and small in the right side.

The artificial samples (figure 1a) are generated using a geo-modeling tool that mimics depositional environment formation based on random walks Massonnat (2019). Horizontal and vertical flipping were performed to increase the samples number from 2,000 to 8,000, this added an additional mode in the training set (i.e., large channel proportion on the right side).

The Brahmaputra river mask was obtained from the supplementary data in Schwenk et al. (2020). The large mask of size 13091×11680 was cropped to images of size 256×256 with a stride of 64 then the cropped images were rotated such that they have vertical alignment with the central line of the large mask. The central line is computed using RivGraph library Schwenk et al. (2020). Horizontal and vertical flipping were also performed to increase the variations in the training set (increasing samples number from 1788 to 7152). All images of the two datasets were resized to 64×64 resolution to match the networks input.

The conditioning maps were calculated at a resolution of 4×4 for all samples. Although they could be calculated at higher resolutions, 4×4 were chosen to mimic the low resolutions usually obtained from seismic surveys. For each sample in the training set, the corresponding map $\mathbf{M}$ is the channel facies proportions in the 4×4 grid (see figures 2 and 3).

2.3 Implementation Details

All models are based on the ResNet architecture He et al. (2016) following Gulrajani et al. (2017). We apply spectral normalization to the discriminator's weights Miyato et al. (2018) and the self-attention mechanism H. Zhang et al. (2019) in both the generator and discriminator at an intermediate layer of an 8×8 resolution. For all experiments, the models are trained using the Adam optimizer with fixed learning rate of 0.0002 for both networks and a batch-size of 32. The latent vector z is sampled from a multivariate standard normal distribution of dimension 128. The final checkpoint used is based on an

exponential moving average of the generator weights with a decaying factor of 0.999 following Brock et al. (2018). When updating the generator we used $-\mathbb{E}_{z \sim p_z}[\log(D(G(z)))]$ as proposed in Goodfellow et al. (2014).

3   Simulation results

Results on the artificial dataset and the Brahmaputra river masks are shown in figures 2 and 3, respectively. The leftmost column shows the conditioning maps $\mathbf{M}$, the middle columns are the corresponding generated images $G(z, \mathbf{M})$ and rightmost column shows the mean per pixel maps calculated over 2,000 generated samples

For each row, we used the same conditioning map and different z vectors. As shown, the generated realizations exhibit variability due to the randomness of z but overall respect the conditioning map.

As shown, the models were able to generalize successfully to modes never seen in the training datasets for both cases. From the visualization perspective, the generated samples at all modes are geologically-plausible. For example, the channels connectivity is maintained for both datasets as well as the models were able to generate levees surrounding the channels for the artificial samples irrespective of the location of the channels which is an indication that the models has not memorized the training samples.

To demonstrate the correlation between the target proportions in the maps and the corresponding generated proportions for the channel facies, figures 4 and 5 show different cross plots where each plot represents proportions of each section in the 4×4 grid. As shown in both figures, the correlation between the target and the generated proportions is strong with an R^2 value of almost 1.

The models were able to extrapolate to unseen range of proportions (the red dots in figure 4) in the artificial training set while the proportions for the entire range $[0, 1]$ were represented in the real dataset. The unrepresented realizations can then be understood from two perspectives:

1. The model can generalize to unseen proportions within each section in the grid as shown in figure 4.

2. The model can generalize to unseen non-stationary patterns over the whole image (combining structures from patches not in the training set) as shown in figures 2 and 3.

We also calculated the two-point probability function which measures the probability that two points, separated by a given distance, have the same channel facies as shown in figure 6. The function is computed for only two sections (the top left section and the section at the second row and the second column) in the 4×4 grid for each dataset at 4 different conditions. Figures 6a and 6b show the probability functions for the artificial dataset and figures 6c and 6d are for the real binary masks dataset. As shown, the function for the generated samples (i.e., the solid lines) is consistent with the one for the training samples (i.e., dashed lines). The generalization capability of the model is demonstrated at some unrepresented conditions (e.g., 80% in figure 6a and 60% and 80% in figure 6b) where the functions follow the general trend. At large distance, the functions mismatch increases, this could be due to the fact that the model tries to adjust the geological consistency at the boundaries which might be different from the training samples.

Due to the convolutional nature of the conditioning method, after training we can use a conditioning map of a higher resolution than the one used when training. In figure 7, we show realizations generated using conditioning maps with resolutions of 4×4, 8×8, 16×16 and 32×32. As shown, despite the fact that the model has been trained only on 4×4 maps, it is still able to generate plausible realizations using maps of higher resolutions.

4   Conclusion

In this work, we investigate the generalization ability of GANs models to generate unrepresented non-stationary realizations. The conditioning algorithm used allowed the model to learn the spatial
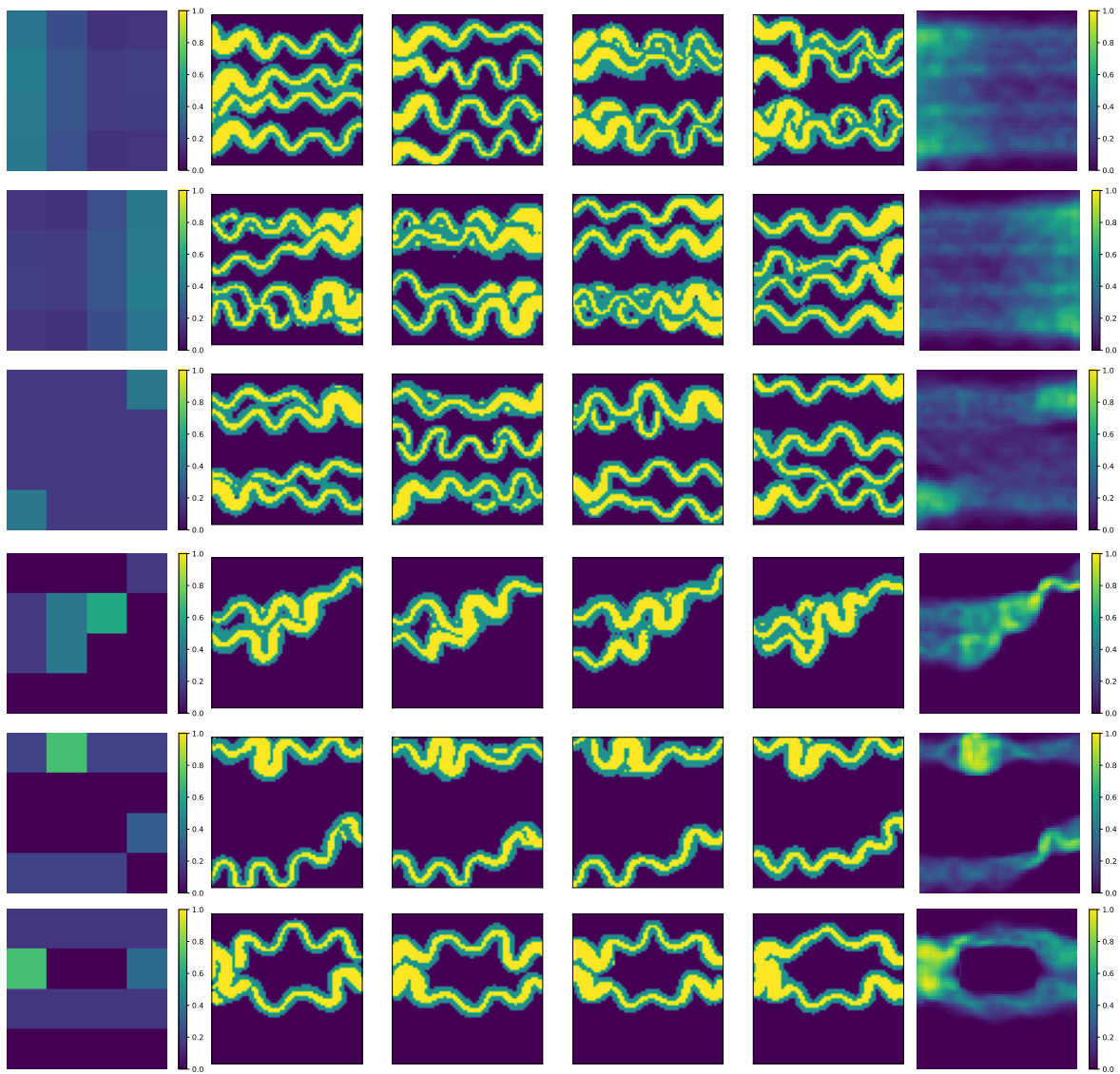
Figure 2: Generated non-stationary realizations on the artificial dataset: the input conditioning maps are in the leftmost columns, the middle columns are the generated samples and the per-pixel mean maps are in the rightmost columns.
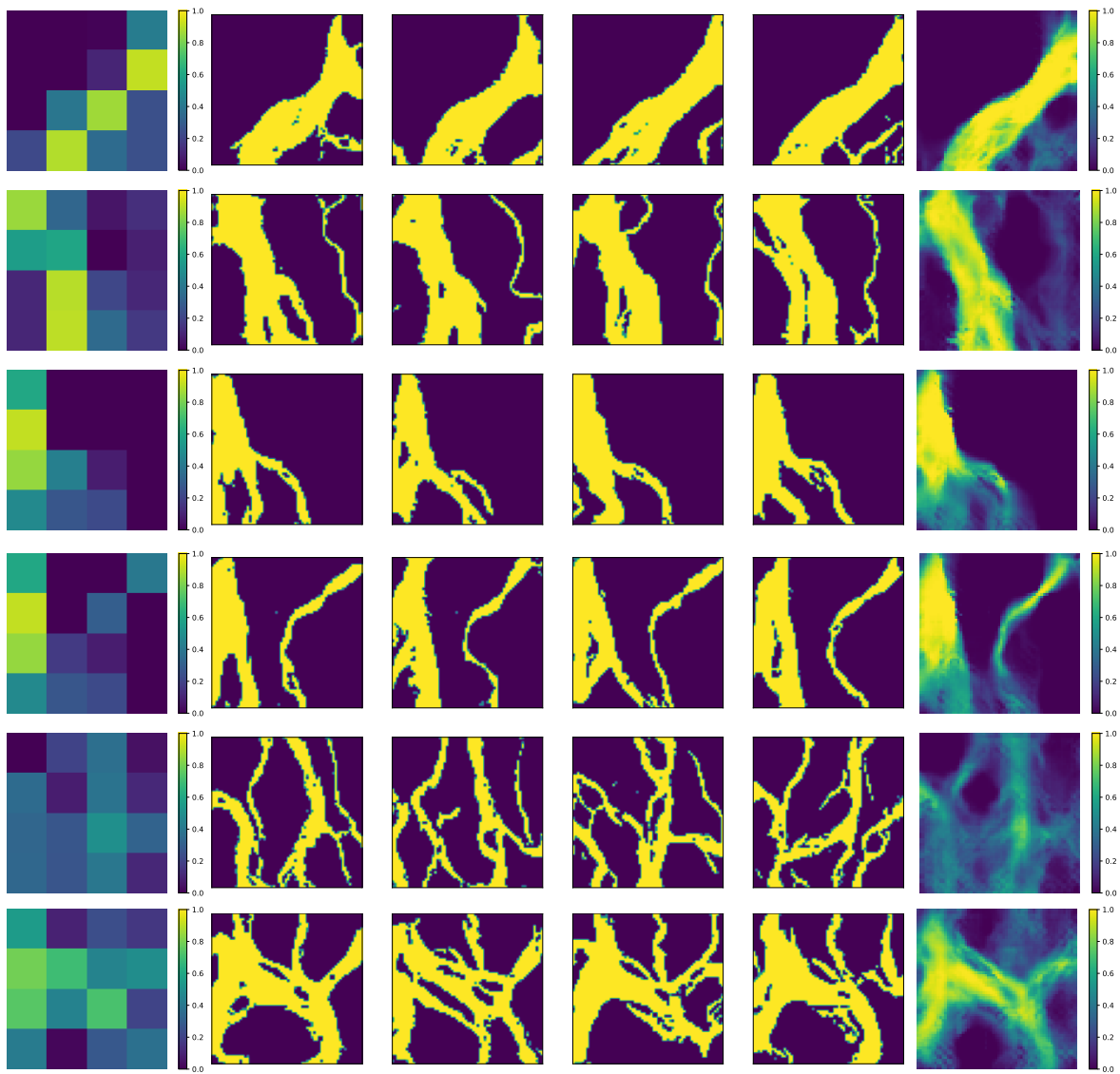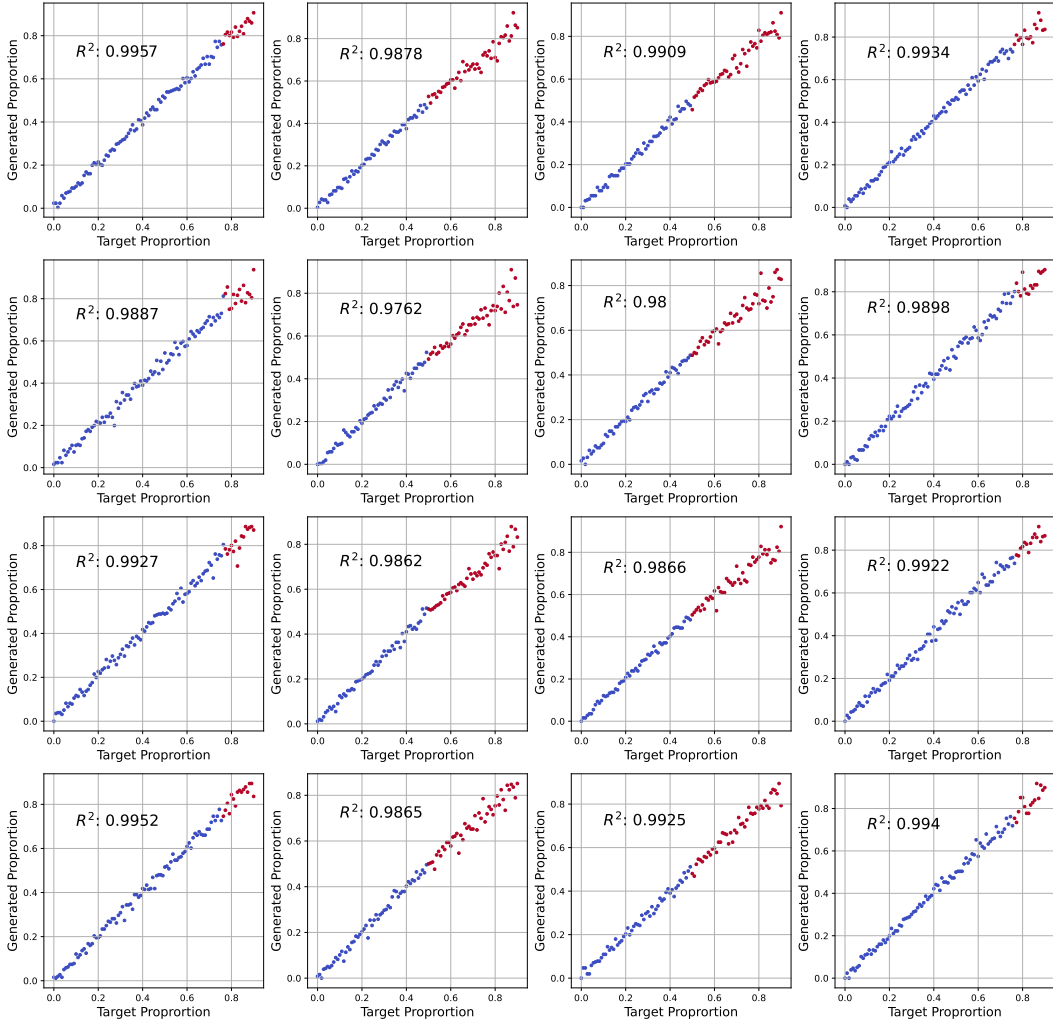
Figure 3: Generated non-stationary realizations on the real masks of the Brahmaputra river: the input conditioning maps are in the leftmost columns, the middle columns are the generated samples and the per-pixel mean maps are in the rightmost columns.

Figure 4: Cross plots between the generated channel proportions and target proportions in the 4×4 conditioning maps for the artificial dataset. In each plot, we change the corresponding value in the map and fix all the other values. The blue dots lie within the represented range in the training set while the red ones lie beyond the seen range.
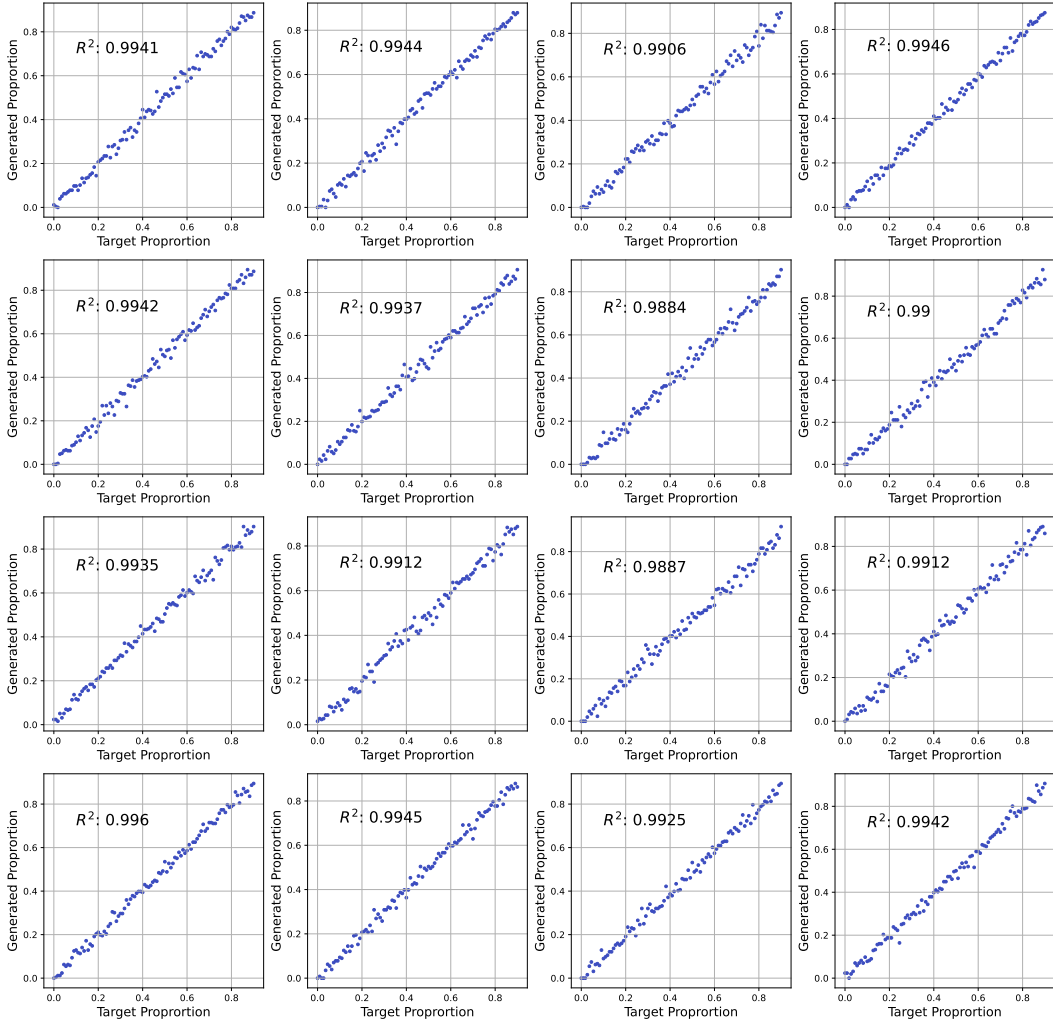
Figure 5: Cross plots between the generated channel proportions and target proportions in the 4×4 conditioning maps for the real masks dataset. In each plot, we change the corresponding value in the map and fix all the other values. Notice that all points are blue as the training proportions cover the whole range $[0, 1]$.
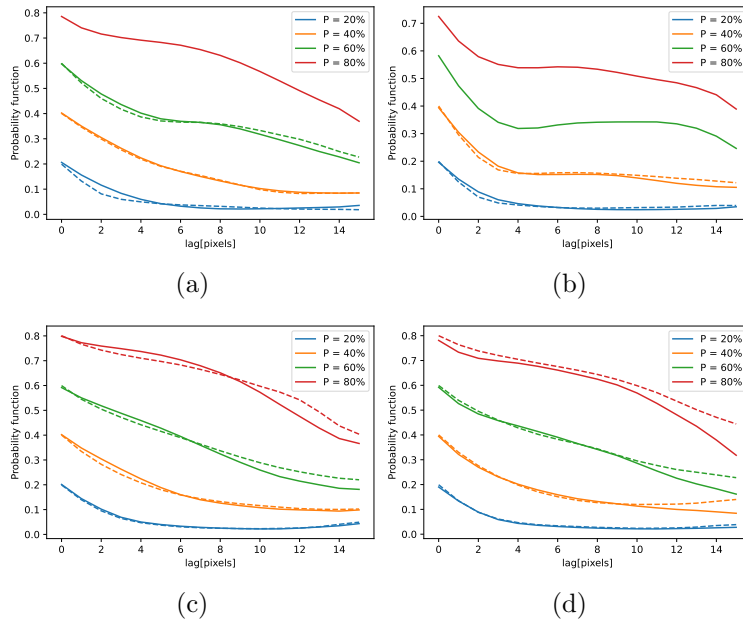
Figure 6: Two-point probability functions. The dashed lines indicate calculations from the training samples at the same proportions while the solid lines are for the generated samples. The computation was done for two sections in the 4×4 grid for each dataset. Figures (a) and (b) show the probability functions calculated for the artificial dataset while figures (c) and (d) show the probability functions for the real binary masks.

correlations between the target maps and the generated realizations. Our models were able to generate consistent realizations with spatial maps not represented in the training sets on two cases representing both artificial and real geological samples. Future work might include generating non-stationary data from stationary training sets and extending the work to three dimensional stochastic fields.

5   Acknowledgment

References

Abdellatif, A., Elsheikh, A. H., Graham, G., Busby, D., & Berthet, P. (2022). Generating unrepresented proportions of geological facies using generative adversarial networks. *Computers and Geosciences*, 105085. doi: https://doi.org/10.1016/j.cageo.2022.105085

Brock, A., Donahue, J., & Simonyan, K. (2018). Large scale GAN training for high fidelity natural image synthesis. *arXiv preprint arXiv:1809.11096*.

Chan, S., & Elsheikh, A. H. (2017). Parametrization and generation of geological models with generative adversarial networks. *arXiv preprint arXiv:1708.01810*.

Chan, S., & Elsheikh, A. H. (2019). Parametric generation of conditional geological realizations using generative neural networks. *Computational Geosciences*, *23*(5), 925–952.
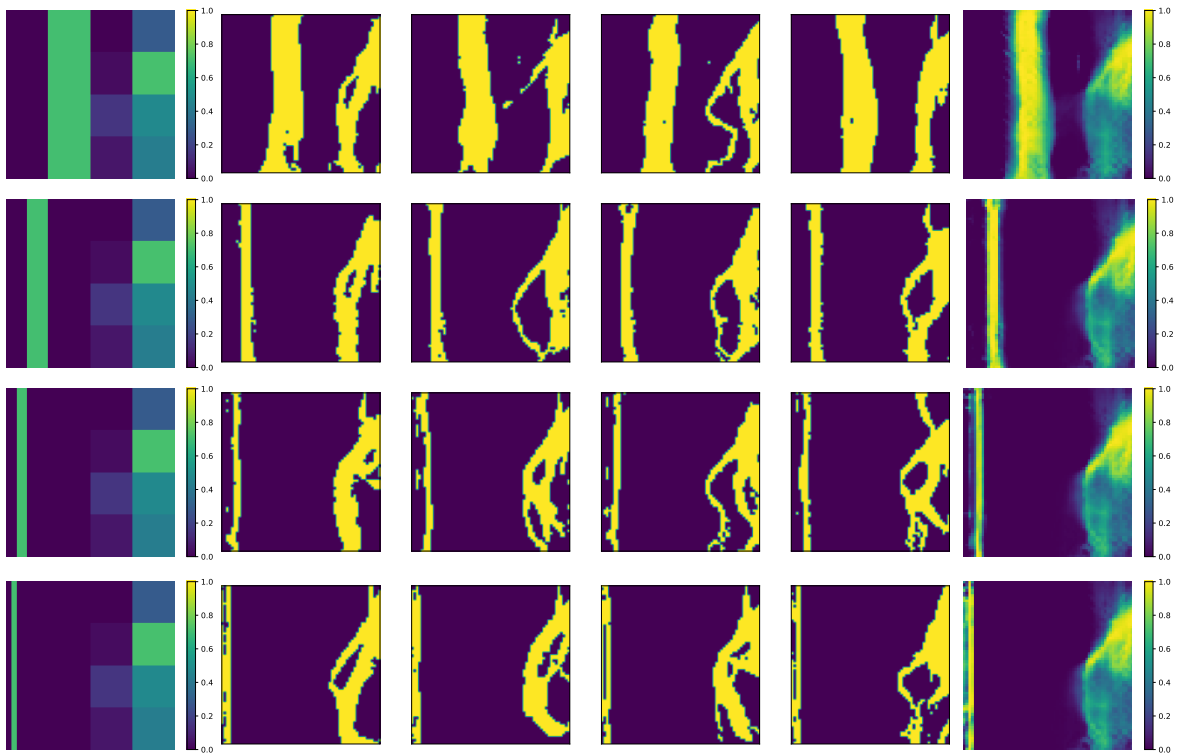
Figure 7: Conditioning realization to high resolution maps. Maps of resolutions 4×4, 8×8, 16×16 and 32×32 are used in the first, second, third and forth columns, respectively.

Dupont, E., Zhang, T., Tilke, P., Liang, L., & Bailey, W. (2018). Generating realistic geology conditioned on physical measurements with generative adversarial networks. *arXiv preprint arXiv:1802.03065*.

Emery, X., & Lantuéjoul, C. (2014). Can a training image be a substitute for a random field model? *Mathematical Geosciences*, *46*(2), 133–147.

Goodfellow, I., Pouget-Abadie, J., Mirza, M., Xu, B., Warde-Farley, D., Ozair, S., ... Bengio, Y. (2014). Generative adversarial nets. In *Advances in neural information processing systems* (pp. 2672–2680).

Gulrajani, I., Ahmed, F., Arjovsky, M., Dumoulin, V., & Courville, A. C. (2017). Improved training of Wasserstein GANs. In *Advances in neural information processing systems* (pp. 5767–5777).

He, K., Zhang, X., Ren, S., & Sun, J. (2016). Deep residual learning for image recognition. In *Proceedings of the ieee conference on computer vision and pattern recognition* (pp. 770–778).

Laloy, E., Hérault, R., Jacques, D., & Linde, N. (2018). Training-image based geostatistical inversion using a spatial generative adversarial neural network. *Water Resources Research*, *54*(1), 381–406.

Li, X., Mariethoz, G., Lu, D., & Linde, N. (2016). Patch-based iterative conditional geostatistical simulation using graph cuts. *Water Resources Research*, *52*(8), 6297–6320.

Mariethoz, G., Renard, P., & Straubhaar, J. (2010). The direct sampling method to perform multiple-point geostatistical simulations. *Water Resources Research*, *46*(11).

Massonnat, G. (2019). Random walk for simulation of geobodies: A new process-like methodology for reservoir modelling. In *Petroleum geostatistics 2019* (Vol. 2019, pp. 1–5).

Mirza, M., & Osindero, S. (2014). Conditional generative adversarial nets. *arXiv preprint arXiv:1411.1784*.

Miyato, T., Kataoka, T., Koyama, M., & Yoshida, Y. (2018). Spectral normalization for generative adversarial networks. *arXiv preprint arXiv:1802.05957*.

Mosser, L., Dubrule, O., & Blunt, M. J. (2017). Reconstruction of three-dimensional porous media using generative adversarial neural networks. *Physical Review E*, *96*(4), 043309.

Mosser, L., Kimman, W., Dramsch, J., Purves, S., De la Fuente Briceño, A., & Ganssle, G. (2018). Rapid seismic domain transfer: Seismic velocity inversion and modeling using deep generative neural networks. In *80th eage conference and exhibition 2018* (Vol. 2018, pp. 1–5).

Nesvold, E., & Mukerji, T. (2019). Geomodeling using generative adversarial networks and a database of satellite imagery of modern river deltas. In *Petroleum geostatistics 2019* (Vol. 2019, pp. 1–5).

Park, T., Liu, M.-Y., Wang, T.-C., & Zhu, J.-Y. (2019). Semantic image synthesis with spatially-adaptive normalization. In *Proceedings of the ieee conference on computer vision and pattern recognition* (pp. 2337–2346).

Ronneberger, O., Fischer, P., & Brox, T. (2015). U-net: Convolutional networks for biomedical image segmentation. In *International conference on medical image computing and computer-assisted intervention* (pp. 234–241).

Schwenk, J., Piliouras, A., & Rowland, J. C. (2020). Determining flow directions in river channel networks using planform morphology and topology. *Earth Surface Dynamics*, *8*(1), 87–102.

Song, S., Mukerji, T., & Hou, J. (2021a). Bridging the gap between geophysics and geology with generative adversarial networks. *IEEE Transactions on Geoscience and Remote Sensing*.

Song, S., Mukerji, T., & Hou, J. (2021b). GANSim: Conditional facies simulation using an improved progressive growing of generative adversarial networks (GANs). *Mathematical Geosciences*, 1–32.

Strebelle, S. (2002). Conditional simulation of complex geological structures using multiple-point statistics. *Mathematical geology*, *34*(1), 1–21.

Sun, A. Y. (2018). Discovering state-parameter mappings in subsurface models using generative adversarial networks. *Geophysical Research Letters*, *45*(20), 11–137.

Zhang, H., Goodfellow, I., Metaxas, D., & Odena, A. (2019). Self-attention generative adversarial networks. In *International conference on machine learning* (pp. 7354–7363).

Zhang, T., Tilke, P., Dupont, E., Zhu, L., Liang, L., & Bailey, W. (2019). Generating geologically realistic 3d reservoir facies models using deep learning of sedimentary architecture with generative adversarial networks. In *International petroleum technology conference.*

Zhong, Z., Sun, A. Y., & Jeong, H. (2019). Predicting CO_2 plume migration in heterogeneous formations using conditional deep convolutional generative adversarial network. *Water Resources Research*, *55*(7), 5830–5851.

Zhu, J.-Y., Park, T., Isola, P., & Efros, A. A. (2017). Unpaired image-to-image translation using cycle-consistent adversarial networks. In *Proceedings of the ieee international conference on computer vision* (pp. 2223–2232).